Supporting Information

Tuning the Optical and Magnetic Properties of Lanthanide Single-Ion Magnets using Nitro-functionalized Trispyrazolylborates

Christopher Hossack,[1] Folasade Abdul,[1] Christopher Cahill,[1] Claire Besson[1,*]

Table of Contents

Single Crystal Diffraction Data

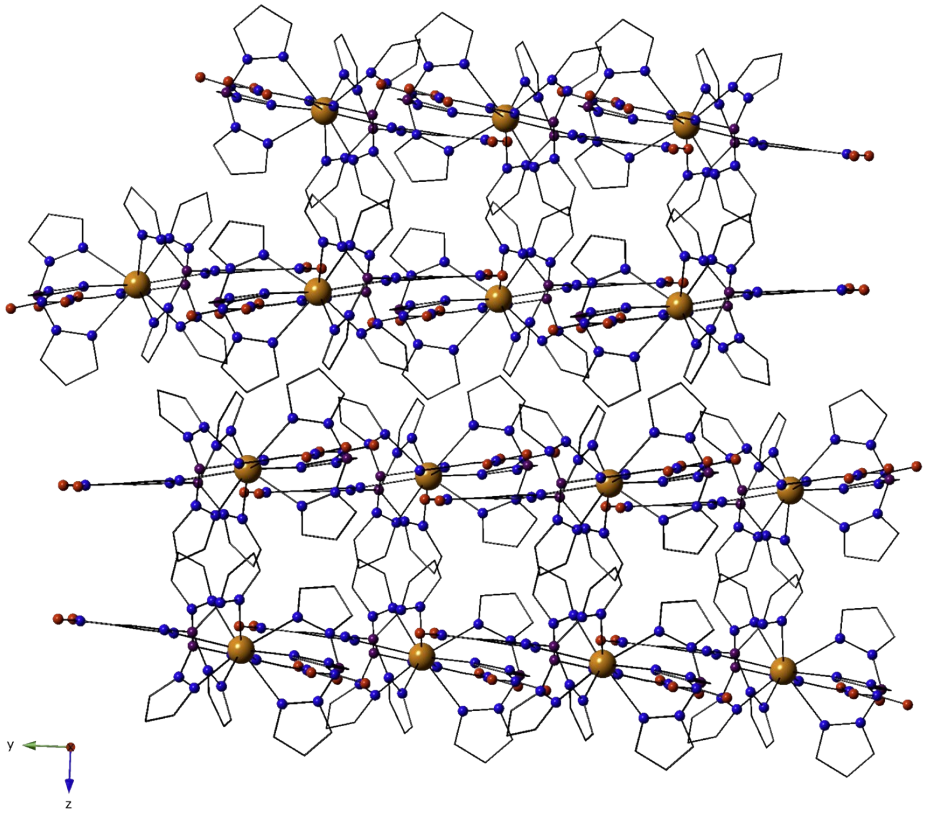

Figure S1: Packing diagram of $Ln(4\text{-}NO_2Tp)_3{\cdot}C_6H_{14}$ polymorph (disordered hexane molecules were omitted for clarity) along [001] direction with hydrogen bonded sheets of $Ln(4\text{-}NO_2Tp)_3$ monomers stacking in a ABBA arrangement.

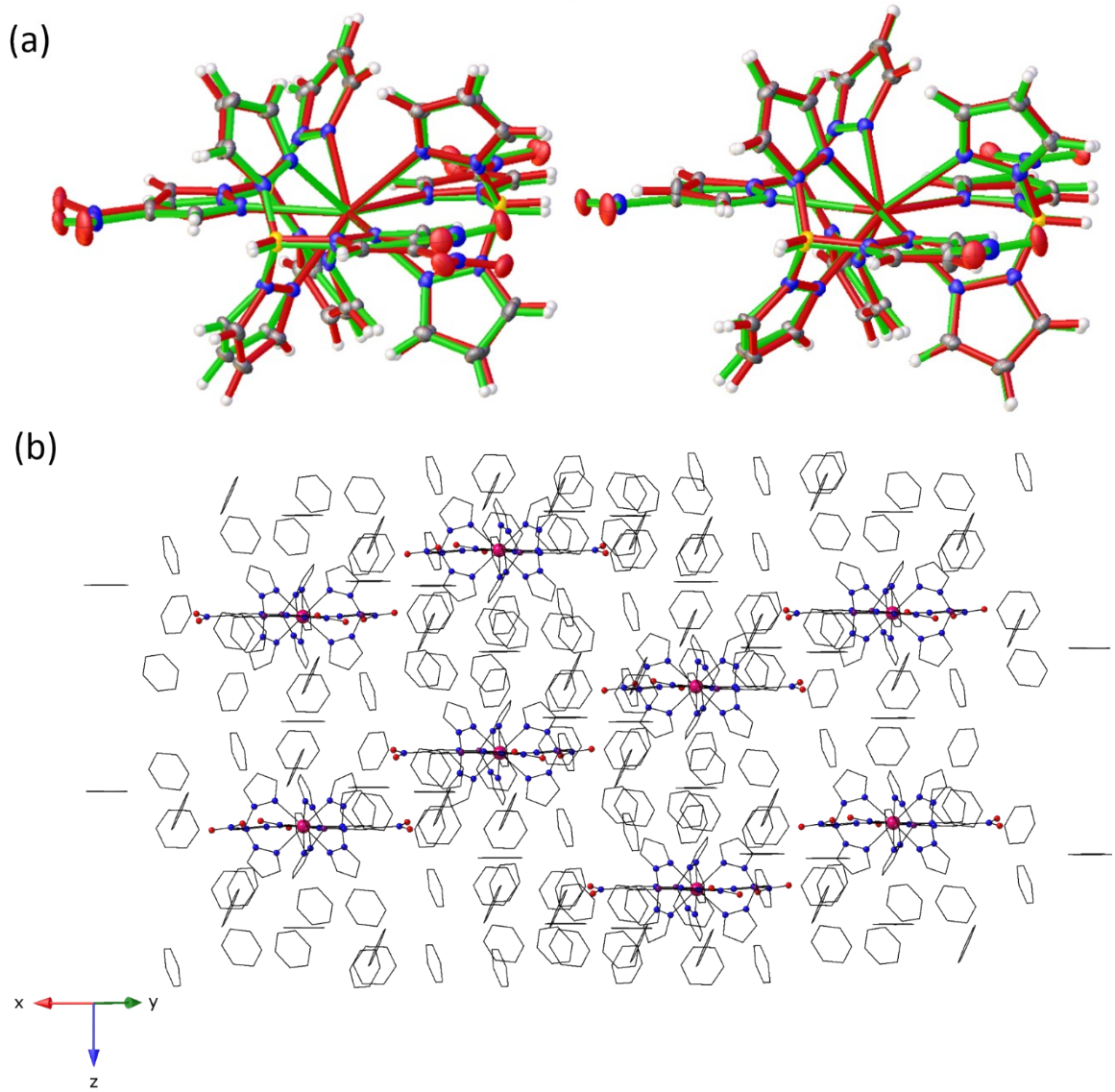

Figure S2: (a) Superposition of the structures of **5a** (green), **5b** (left, red) and $[SmTp_3]$[1] (right, red). (b) Packing diagram of **5b** with benzene molecules displayed.

Powder X-Ray Diffraction Patterns

Compounds **1a** – **9a**

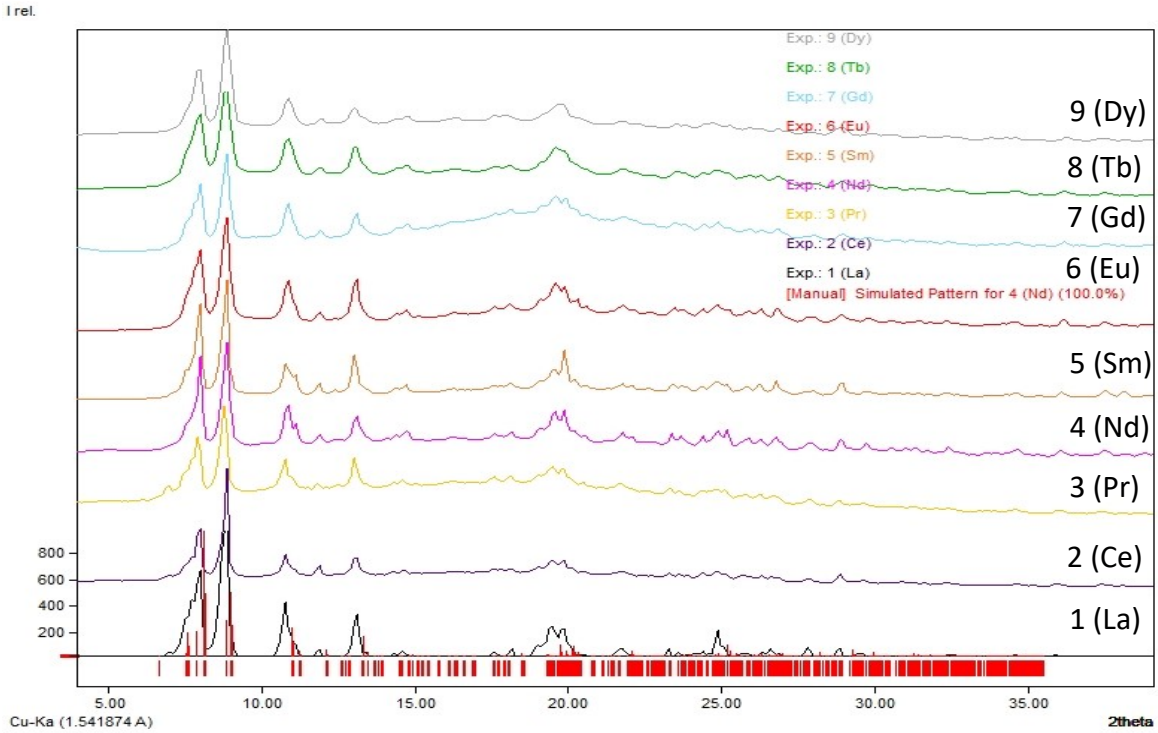

Figure S3: PXRD patterns of isomorphous compounds, a**1** – **9a** with the simulated pattern of **4a** (red lines).

Compounds **5b** and **8b**

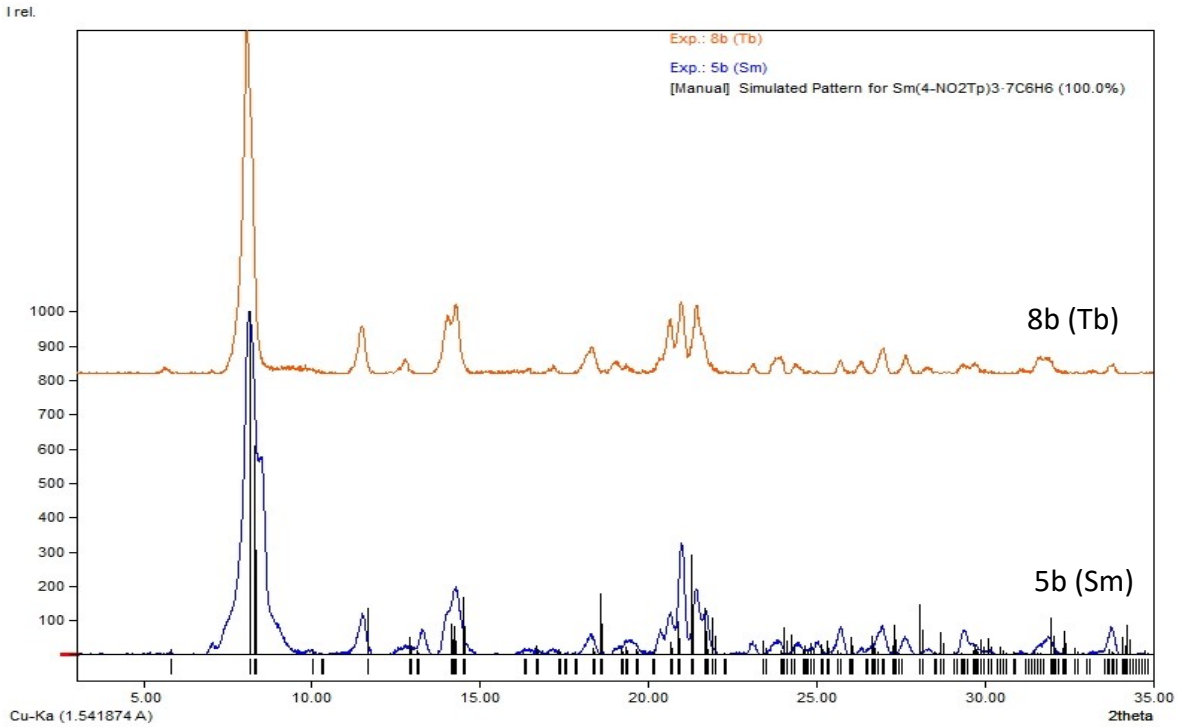

Figure S4: PXRD patterns of **5b** and **8b** with the simulated pattern of **5b** (black lines).

Infrared Spectra

Compounds **1a** – **9a**

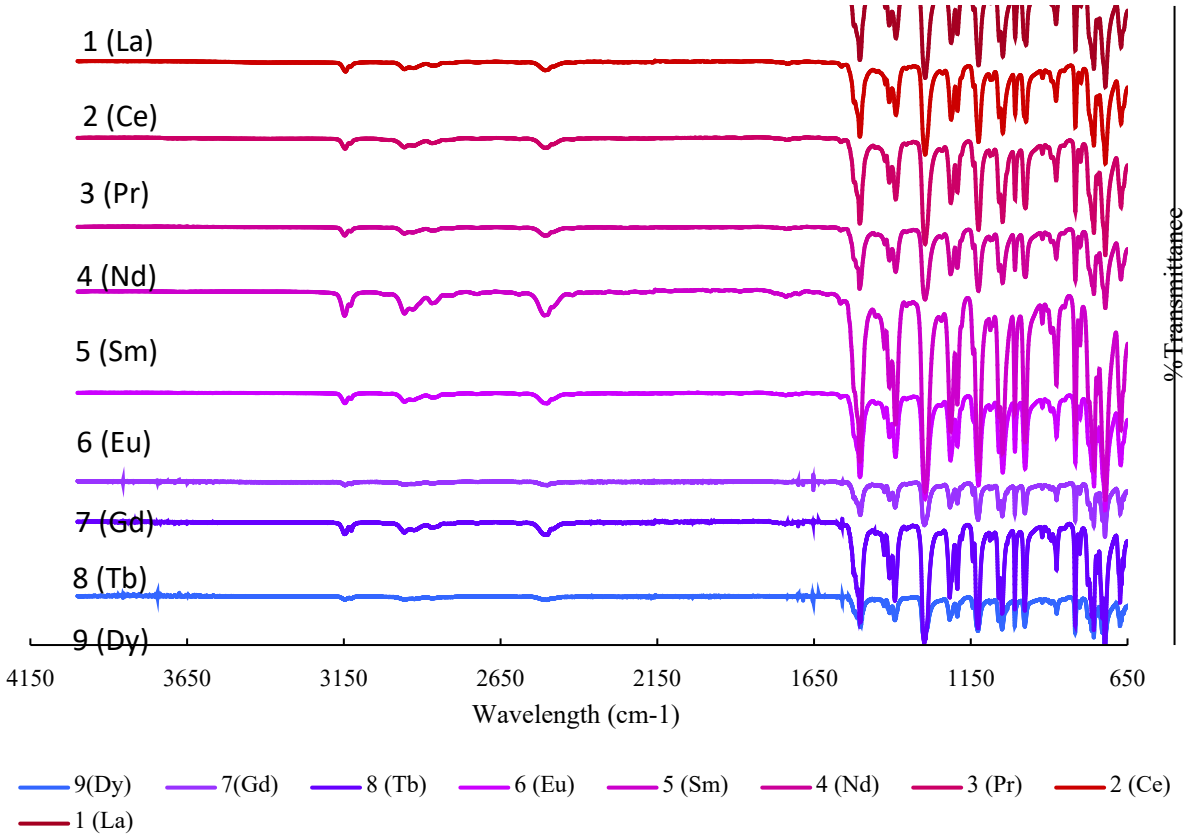

Figure S5: IR spectra (ATR) of **1a** – **9a**, $[Ln(4\text{-}NO_2Tp)_3]\cdot C_6H_{14}$.

Compounds **5b** and **8b**

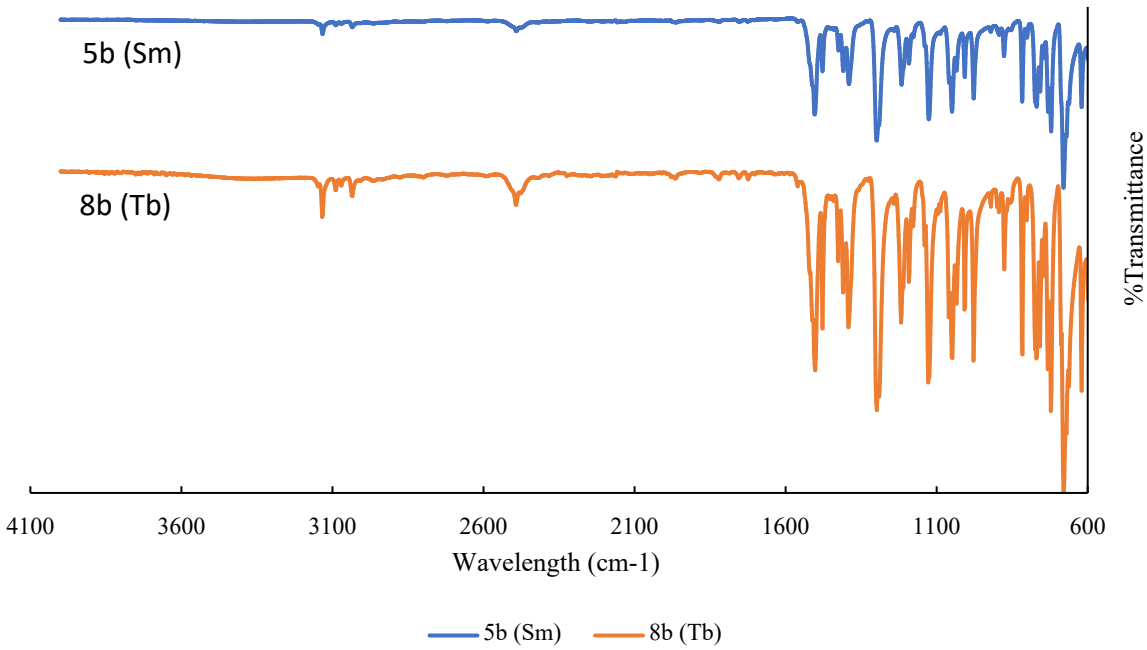

Figure S6: IR spectra (ATR) of **5b** and **8b**, $[Ln(4\text{-}NO_2Tp)_3]\cdot 7\ C_6H_6$.

NMR Spectra

La(4-NO_2Tp)$_3$

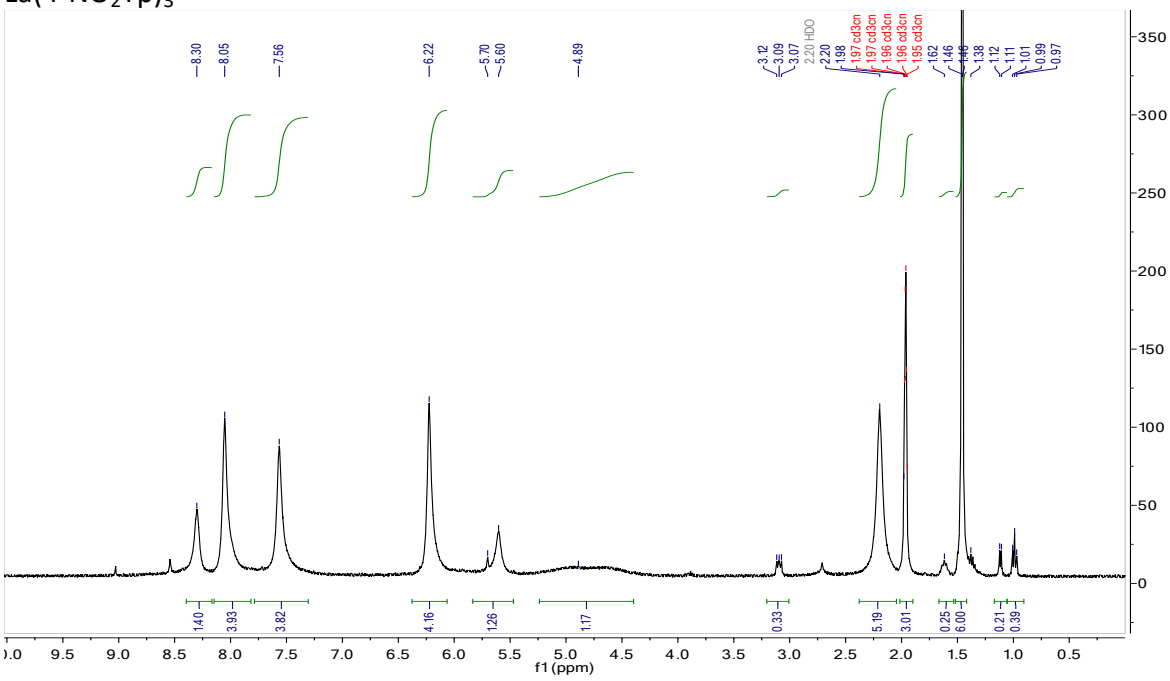

Figure S7: ^{1}H NMR (400 MHz, acetonitrile-d$_3$) of crude La(4-NO_2Tp)$_3$. δ (ppm): 8.30 (s, 1H), 8.05 (s, 2H), 7.56 (s, 2H), 6.22 (s, 2H), 5.65 (d, 1H), 4.89 (s, 1H, BH), 2.20 (HDO), 1.98 (CD_2HCN), 1.52 – 1.42 (cyclohexane). Low intensity peaks at 3.09, 1.62, 1.38 and 0.99 ppm correspond to trace amounts of [TBA]$^+$ from the ligand and at 1.12 ppm to ^{i}PrOH. δ = 8.30, 8.05, 7.56, 6.22, 5.65 ppm correspond to La(4-NO_2Tp)$_3$.

Ce(4-NO_2Tp)$_3$

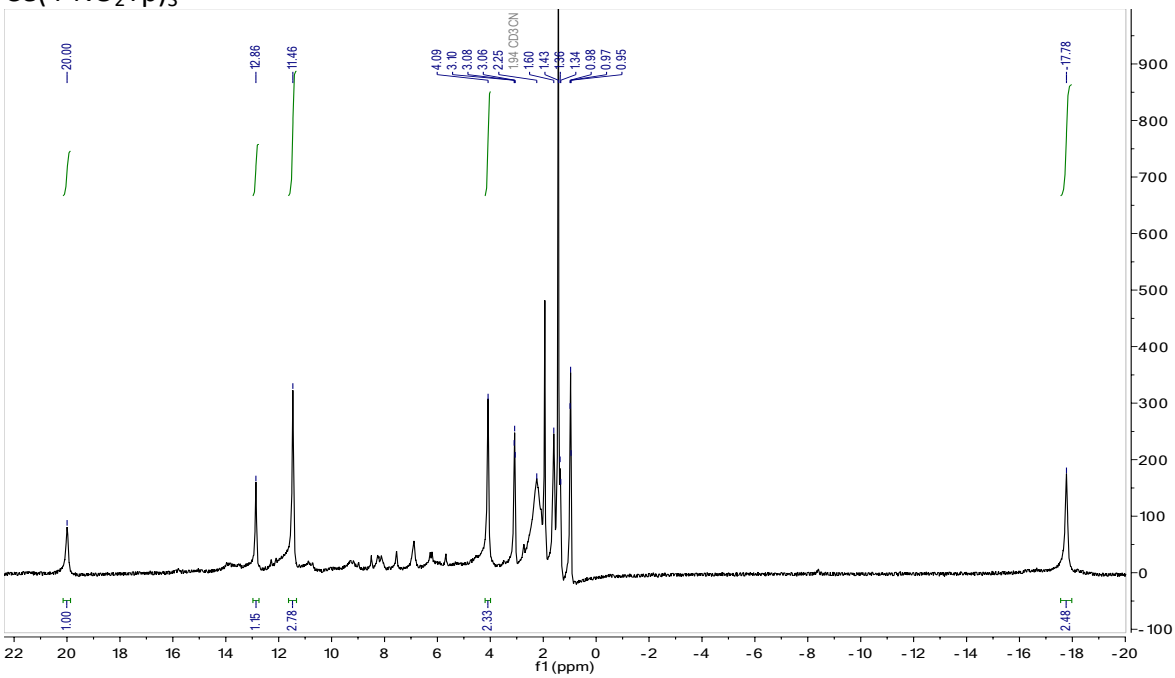

Figure S8: ^{1}H NMR (400 MHz, acetonitrile-d$_3$) of crude Ce(4-NO_2Tp)$_3$. δ (ppm): 20.00 (s, 1H), 12.86 (s, 1H), 11.46 (s, 2H), 4.09 (s, 2H), 2.25 (HDO), 1.94 (CD_2HCN), 1.43 (cyclohexane) and -17.78 (s, 2H). Low intensity peaks between 6 – 8 and at 3.10, 1.60, 1.34 and 0.97 ppm correspond to [TBA][4-NO_2Tp]. δ = 20.00, 12.86, 11.46, 4.09, -17.78 ppm correspond to Ce(4-NO_2Tp)$_3$.

Pr(4-NO_2Tp)$_3$

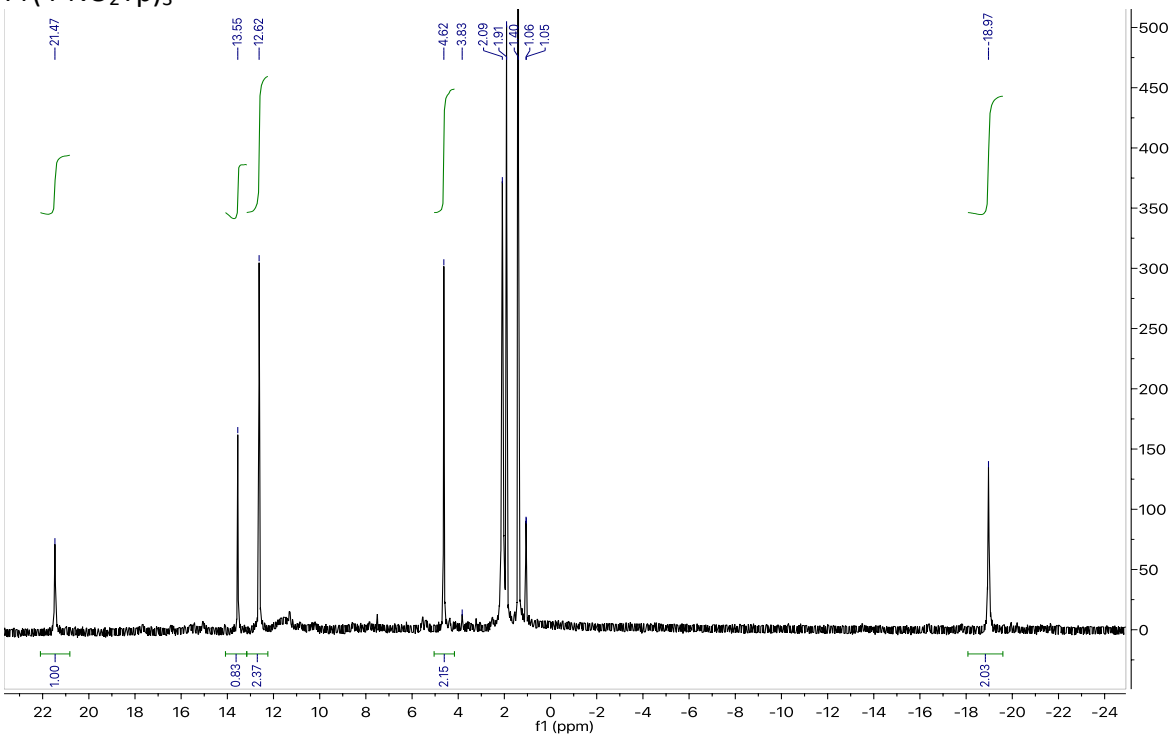

Figure S9: ^{1}H NMR (400 MHz, acetonitrile-d$_3$) of crude Pr(4-NO_2Tp)$_3$. δ (ppm): 21.47 (s, 1H), 13.35 (s, 1H), 12.62 (s, 2H), 4.62 (s, 2H), 2.09 (HDO), 1.91 (CD_2HCN), 1.40 (cyclohexane), 1.06 (^{i}PrOH) and -18.87 (d, 2H). δ = 21.47, 13.35, 12.62, 4.62, -18.87 ppm correspond to Pr(4-NO_2Tp)$_3$.

Nd(4-NO_2Tp)$_3$

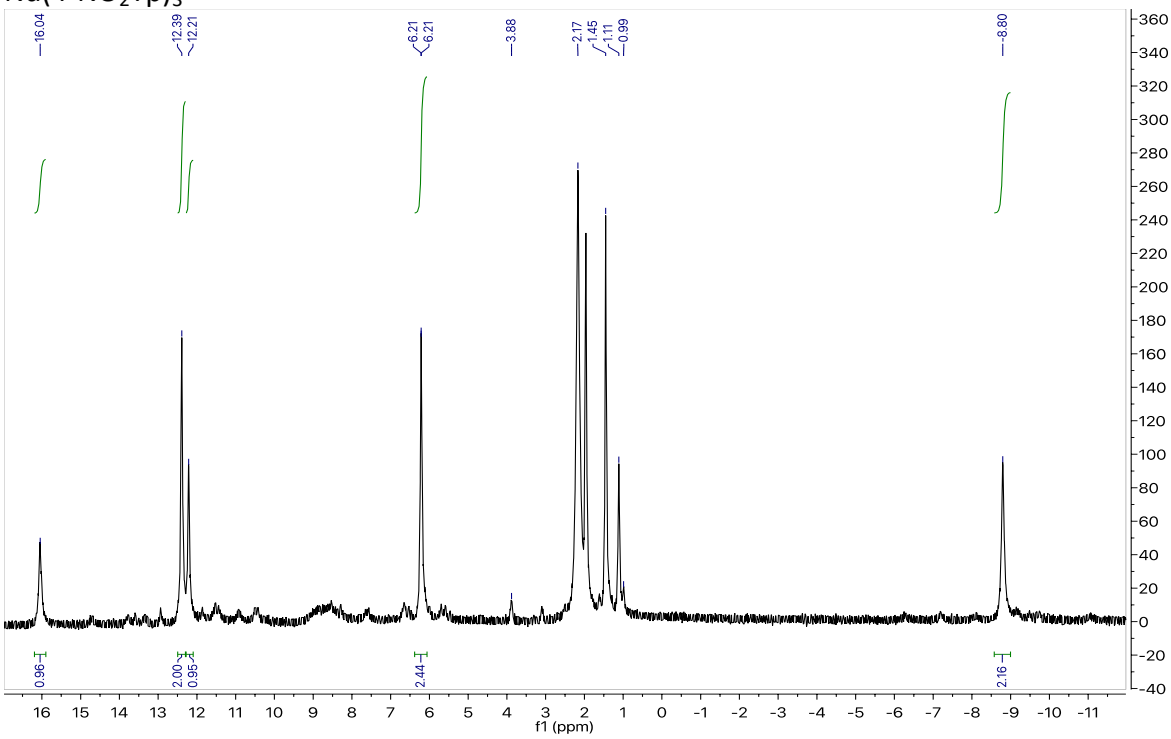

Figure S10: ^{1}H NMR (400 MHz, acetonitrile-d$_3$) of crude Nd(4-NO_2Tp)$_3$. δ (ppm): 16.04 (s, 1H), 12.39 (s, 2H), 12.21 (s, 1H), 6.21 (m, 2H), 3.88 (^{i}PrOH), 2.09 (HDO/CD_2HCN), 1.45 (cyclohexane), 1.11 (^{i}PrOH), 0.99 (residual tetrabutylammonium) and -8.80 (s, 2H). δ = 16.04, 12.39, 12.21, 6.21, -8.80 ppm correspond to Nd(4-NO_2Tp)$_3$.

Sm(4-NO_2Tp)$_3$

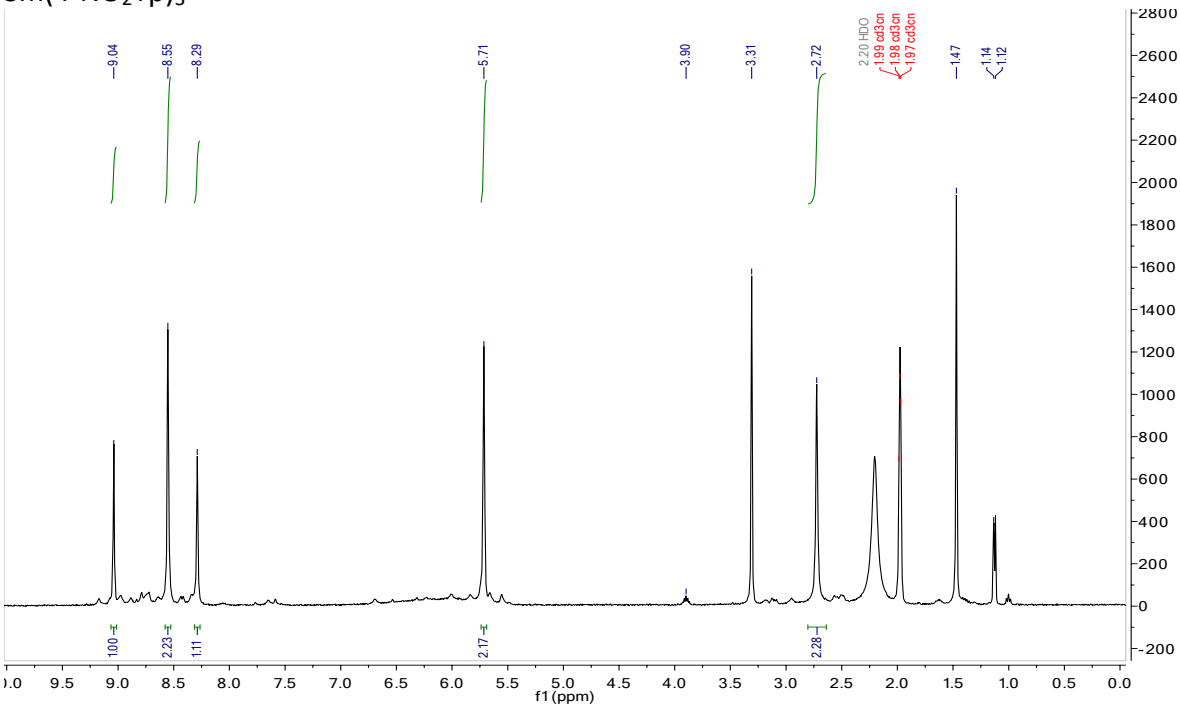

Figure S11: ^{1}H NMR (400 MHz, acetonitrile-d$_3$) of crude Sm(4-NO_2Tp)$_3$. δ (ppm): 9.04 (s, 1H), 8.55 (s, 2H), 8.29 (s, 1H), 5.71 (m, 2H), 3.90 (^{i}PrOH), 3.31 (MeOH), 2.72 (s, 2H), 2.20 (HDO), 1.98 (CD_2HCN), 1.47 (cyclohexane) and 1.11 (^{i}PrOH). δ = 9.04, 8.55, 8.29, 5.71, 2.72 ppm correspond to Sm(4-NO_2Tp)$_3$.

Eu(4-NO_2Tp)$_3$

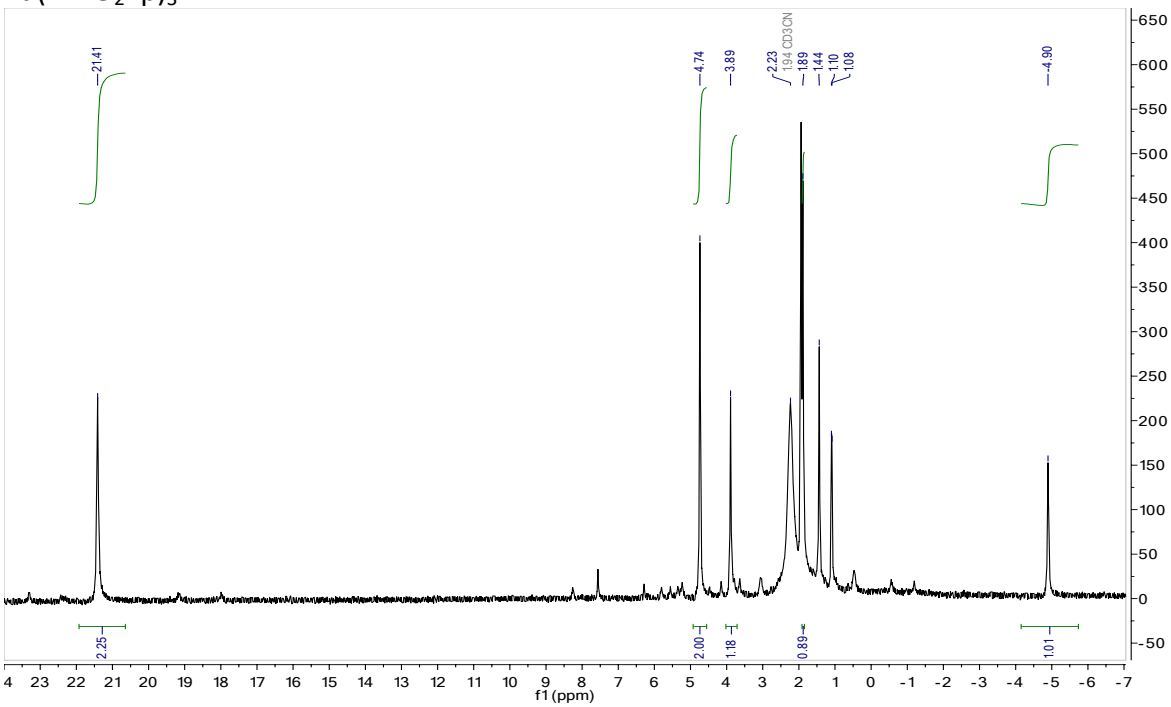

Figure S12: ^{1}H NMR (400 MHz, acetonitrile-d$_3$) of crude Eu(4-NO_2Tp)$_3$. δ (ppm): 21.41 (s, 2H), 4.74 (s, 2H), 3.89 (s, 1H), 2.23 (HDO), 1.94 (CD_2HCN), 1.89 (s, 1H), 1.44 (cyclohexane), 1.10 (^{i}PrOH) and -4.90 (s, 1H). Low intensity peaks correspond to trace amounts of [TBA]$^+$, ^{i}PrOH and MeOH. δ = 21.41, 4.74, 3.89, 1.89, -4.90 ppm correspond to Eu(4-NO_2Tp)$_3$.

$Gd(4\text{-}NO_2Tp)_3$

Relaxation time was too fast to observe the peaks from this complex.

$Tb(4\text{-}NO_2Tp)_3$

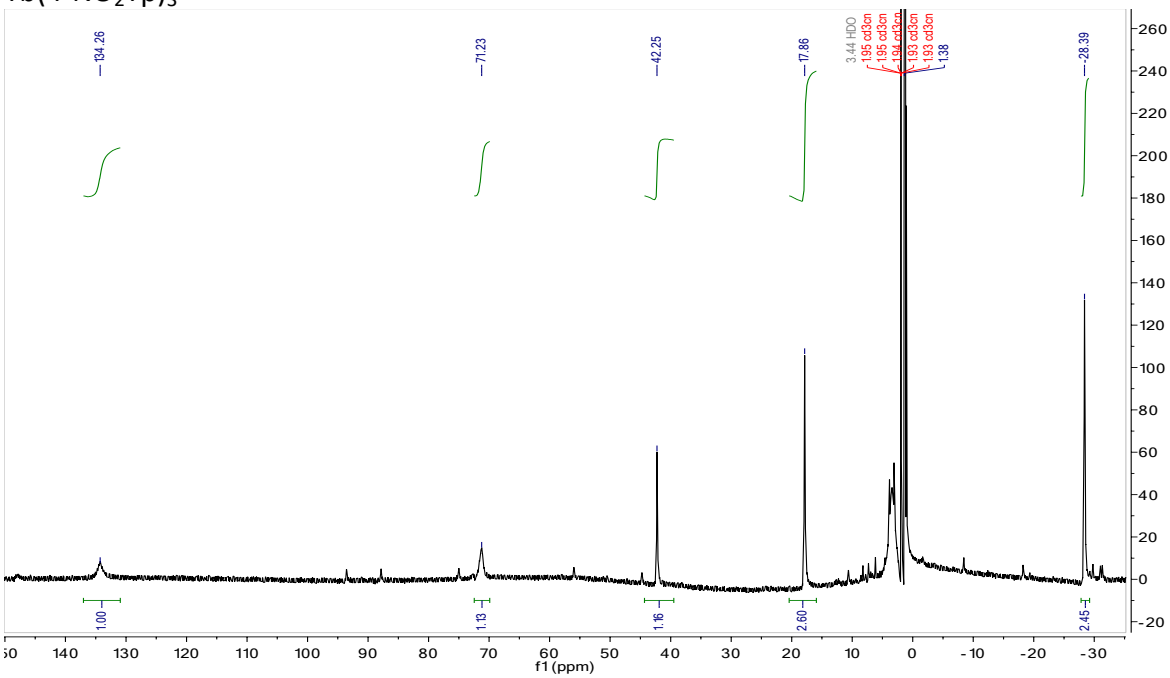

Figure S13: ^{1}H NMR (400 MHz, acetonitrile-d_3) of crude $Tb(4\text{-}NO_2Tp)_3$. δ (ppm): 134.26 (s, 1H), 71.23 (s, 1H), 42.25 (s, 1H), 17.86 (s, 2H), 3.42 (HDO), 1.94 (CD_2HCN), 1.38 (cyclohexane) and -28.39 (s, 2H). Low intensity peaks correspond to trace amounts of $[TBA]^+$, ^{i}PrOH and MeOH. δ = 134.26, 71.23, 42.25, 17.86, -28.39 ppm correspond to $Tb(4\text{-}NO_2Tp)_3$.

$Dy(4\text{-}NO_2Tp)_3$

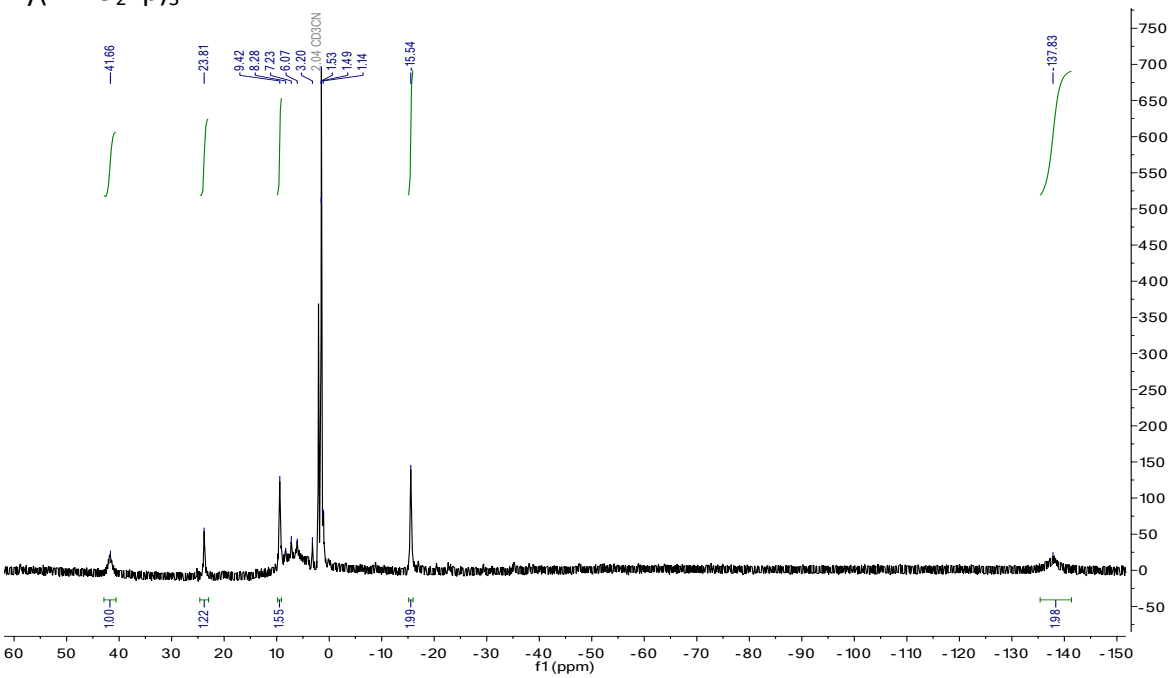

Figure S14: ^{1}H NMR (400 MHz, acetonitrile-d_3) of crude $Dy(4\text{-}NO_2Tp)_3$. δ (ppm) 41.66 (s, 1H), 23.81 (s, 1H), 9.42 (s, 1H), 2.04 (CD_2HCN), 1.49 (cyclohexane), -15.54 (s, 2H) and -137.83 (s, 2H). Low intensity peaks at 8.28, 7.23, 6.07, 3.20, 1.53, and 1.14 ppm correspond to trace amounts of $[TBA][4\text{-}NO_2Tp]$. δ = 41.66, 23.81, 9.42, -15.54 and -137.83 ppm correspond to $Dy(4\text{-}NO_2Tp)_3$.

Thermogravimetric Analysis

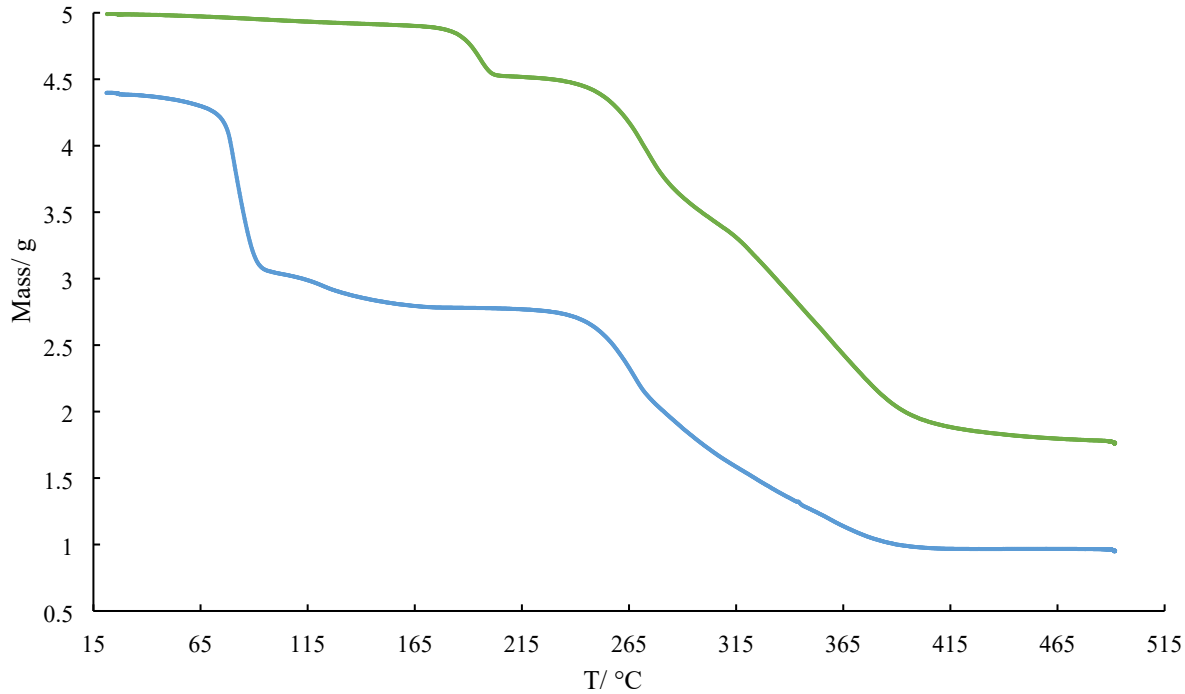

Figure S15: TGA curves of **5a** (top, green) and **5b** (bottom, blue). **5a** features a mass loss of 9 % from 174 – 204 °C assigned as loss of lattice hexanes (*theoretical mass loss = 8.5 %*). **5b** has a major mass loss of 37 % from 70 – 170 °C assigned to the loss of lattice benzene molecules (*theoretical mass loss = 37 %*). Mass losses are consistent with the assigned number of hexanes (1) and benzene (7) in reported chemical formulae.

Diffuse Reflectance Spectra

K[4-NO_2Tp]

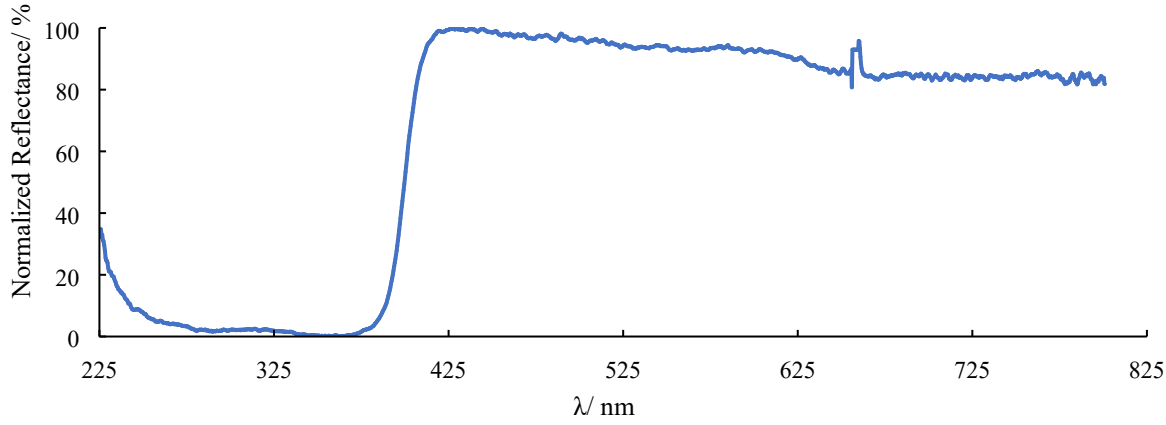

Figure S16: DRS of K[4-NO_2Tp] with absorption band from 225 to 425 nm.

1a

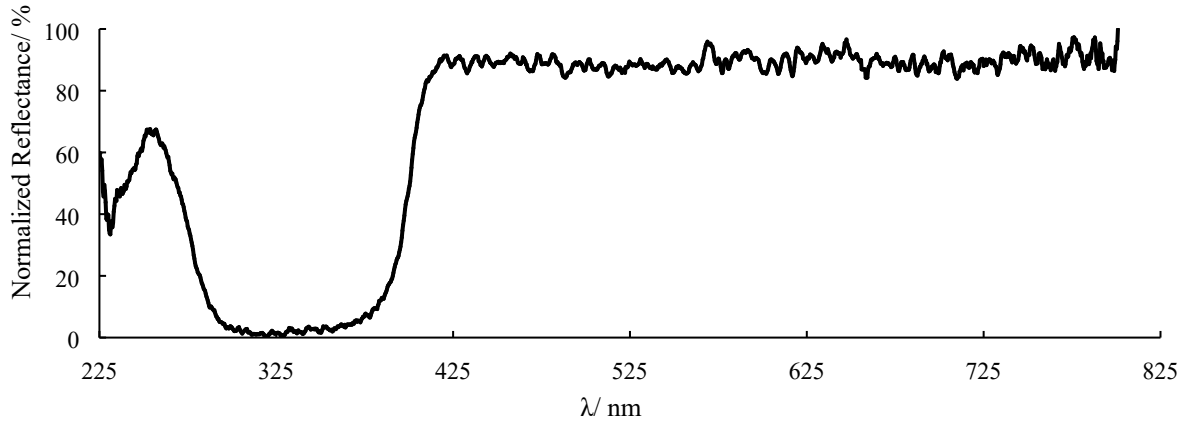

Figure S17: DRS of **1a**(La) with absorption band from 255 to 425 nm.

2a

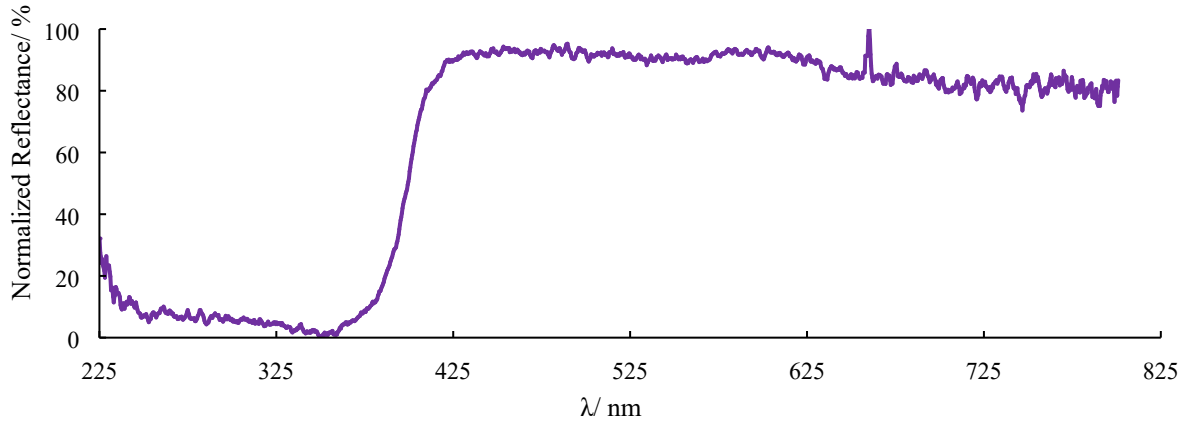

Figure S18: DRS of **2a**(Ce) with absorption band from 225 to 425 nm.

3a

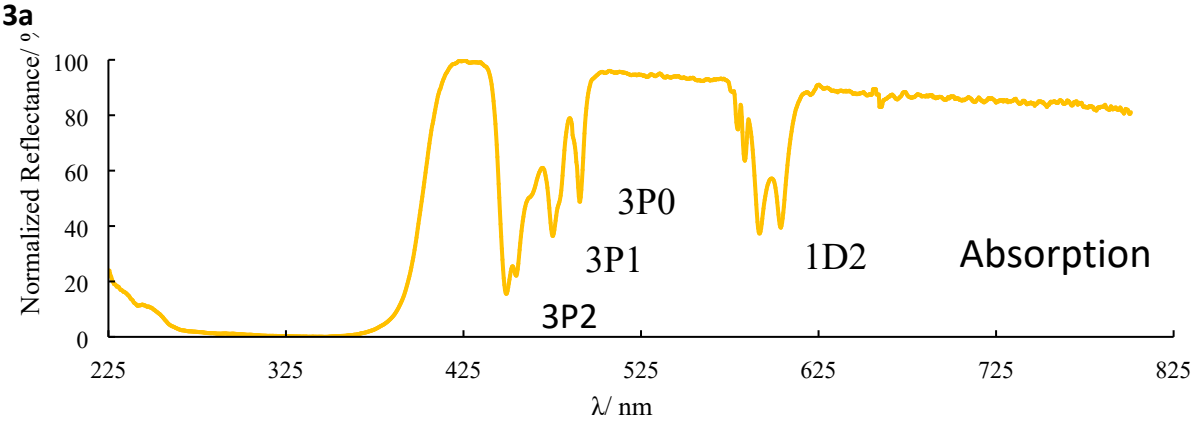

Figure S19: DRS of **3a**(Pr) with absorption band from 225 to 425 nm of 4-NO_2Tp^- with direct Pr^{3+} absorptions from the $^3H_4$ ground state to $^{2S+1}L_J$ at 449 nm ($^3P_0$), 476 nm ($^3P_1$) and 491 nm ($^3P_0$) and 591 and 604 nm ($^1D_2$).

4a

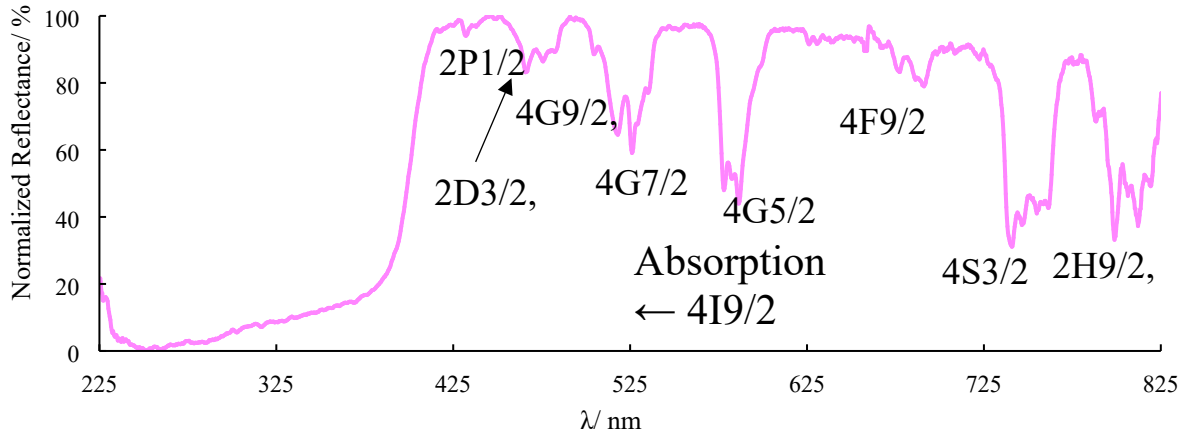

Figure S20: DRS of **4a**(Nd) with absorption band from 225 to 425 nm of 4-NO_2Tp^- with direct Nd^{3+} absorptions from the $^4I_{9/2}$ ground state to $^{2S+1}L_J$ at 432 nm ($^2P_{1/2}$), 466 nm ($^2D_{3/2}$, $^2G_{9/2}$), 525 nm ($^4G_{9/2}$, $^2K_{15/2}$), 527 nm ($^4G_{7/2}$), 587 nm ($^4G_{5/2}$), 692 nm ($^4F_{9/2}$), 740 nm ($^4S_{3/2}$) and 799 nm ($^2H_{9/2}$, $^4F_{5/2}$).

5a

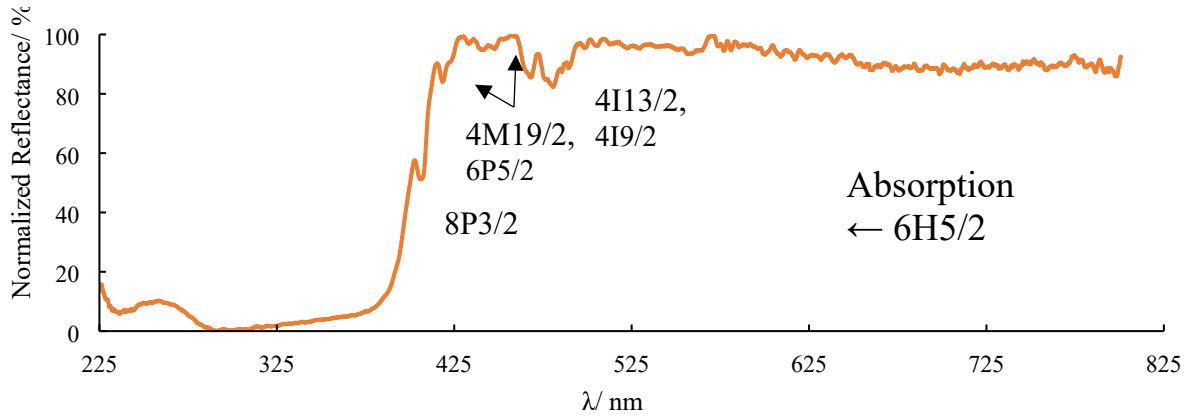

FigureS 21: DRS of **5a**(Sm) with absorption band from 225 to 425 nm of 4-NO_2Tp^- with direct Sm^{3+} absorptions from the $^6H_{5/2}$ ground state to $^{2S+1}L_J$ at 407 nm ($^8P_{3/2}$), 419 nm ($^4M_{19/2}$), 442 nm ($^6P_{5/2}$) and 468 nm ($^4I_{13/2}$) and 480 nm ($^4I_{9/2}$).

6a

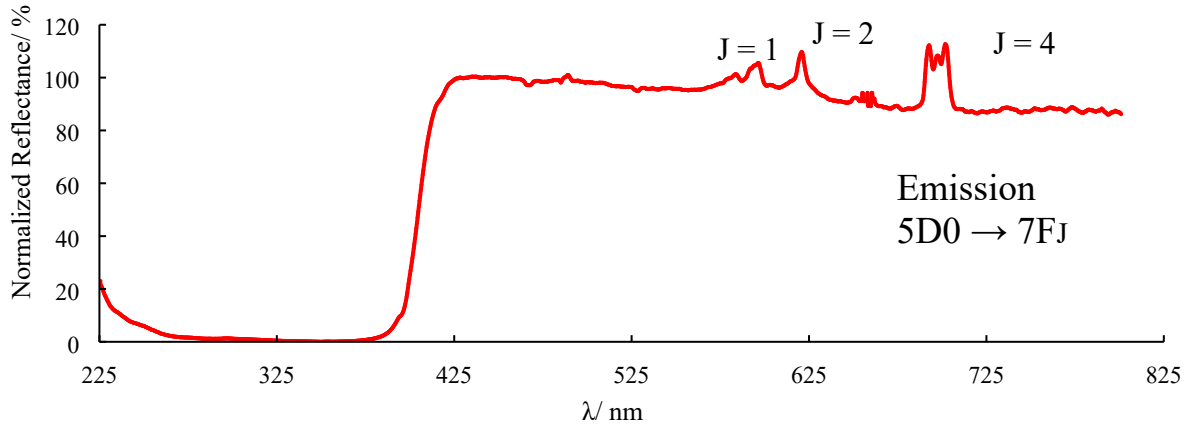

Figure S22: DRS of **6a**(Eu) with absorption band from 225 to 425 nm of 4-NO_2Tp^- with emission from Eu^{3+} ($^5D_0 \rightarrow {}^7F_J$) at 598 nm (J = 1), 622 nm (J = 2) and 693 nm (J = 4).

7a

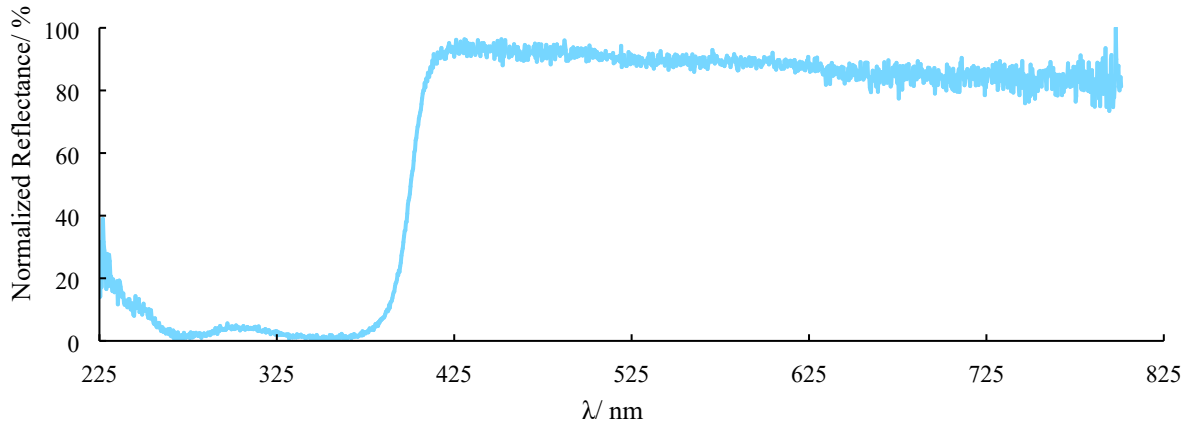

Figure S23: DRS of **7a**(Gd) with absorption band from 225 to 425 nm.

8a

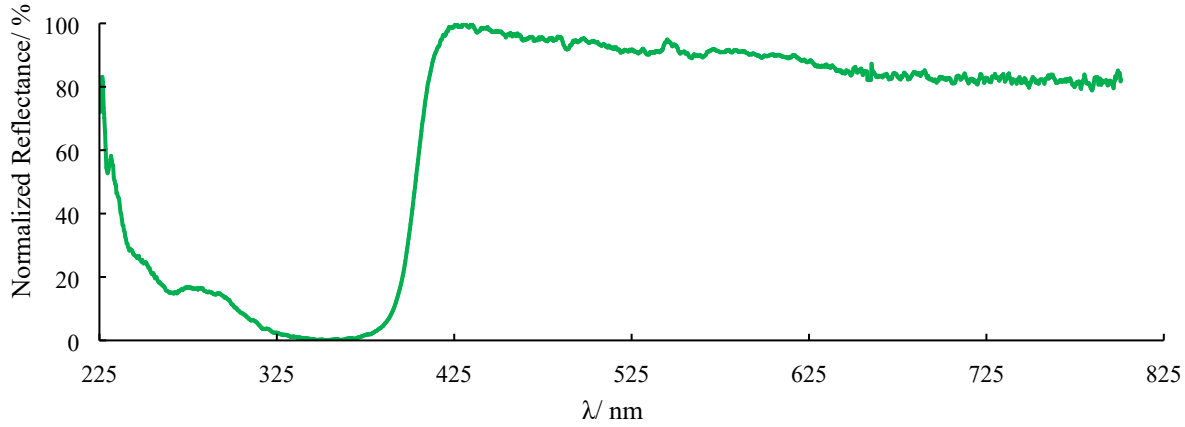

Figure S24: DRS of **8a**(Tb) with absorption band from 225 to 425 nm.

9a

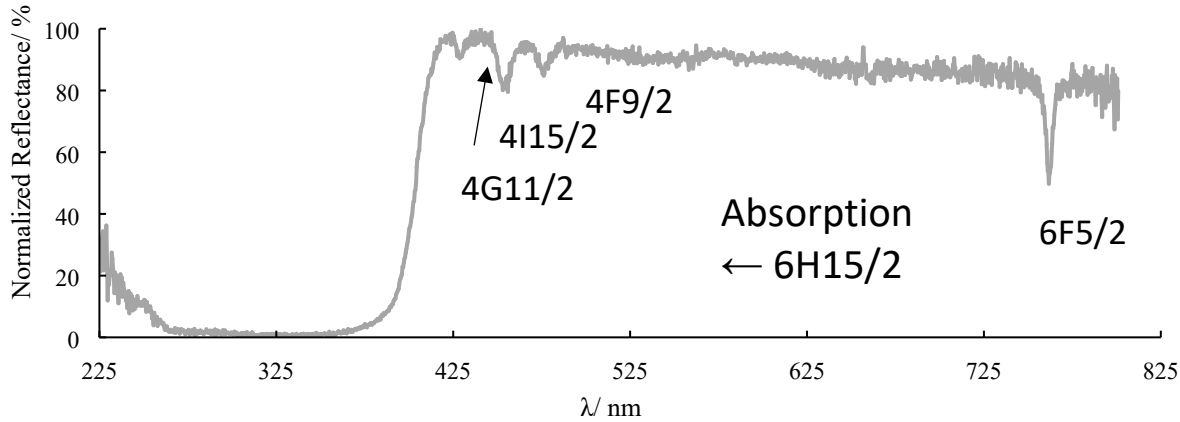

Figure S25: DRS of **9a**(Dy) with absorption band from 225 to 425 nm of 4-NO_2Tp^- with direct Dy^{3+} absorptions from the $^6H_{15/2}$ ground state to $^{2S+1}L_J$ at 429 nm ($^4G_{11/2}$), 456 nm ($^4I_{15/2}$), 476 nm ($^4F_{9/2}$) and 761 nm ($^6F_{5/2}$).

Computational Details

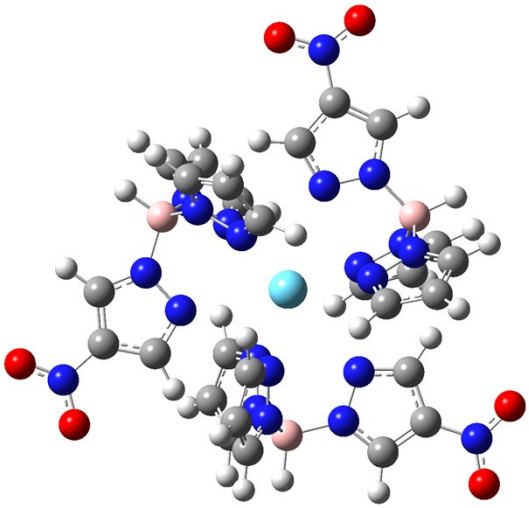

La	9.74887600	5.72414700	17.11949600
C	9.52827200	1.88116400	17.73035400
H	10.60090000	1.84319100	17.66922400
O	10.13837000	-0.86986000	18.11648600
N	7.53346800	2.69744200	17.72863300
B	6.44237600	3.78540900	17.62709300
H	5.36827500	3.27733600	17.77279100
C	8.63535600	0.82444000	17.94931100
O	8.02526100	-1.33347700	18.32081100
N	8.85405700	3.01198000	17.59771200
B	13.12648800	3.84457500	17.20794400
H	14.11740500	3.17437200	17.25245900
B	9.67836400	9.54554500	16.53596600
H	9.76200300	10.72512500	16.34974400
N	6.48693000	4.42387800	16.21554400
O	15.31778300	9.30365700	16.22411600
C	7.37087200	1.38869600	17.94093700

H	6.40388100	0.93639700	18.07088000
C	7.24787100	5.39682700	14.44591600
H	7.95512700	5.92741400	13.82822900
N	7.58433900	5.02455700	15.68312200
O	16.79855700	7.72193500	16.38949300
C	5.93054200	5.03553100	14.15675300
H	5.38099600	5.20095400	13.24699600
N	6.64526400	4.82045900	18.76250900
O	3.78929000	8.73964800	17.02596000
C	5.48693600	4.42034900	15.31108400
H	4.53294600	3.98281700	15.55114800
N	7.78720200	5.53404400	18.94963800
O	4.42220600	10.78924400	16.67882100
C	5.76286400	5.11018700	19.74000000
H	4.79547000	4.63819000	19.76204500
N	12.57604300	6.29152800	16.85482100
C	6.33148600	6.03855400	20.59005900
H	5.89361100	6.48268300	21.46642000
N	13.52309400	5.31523400	16.95440500
N	8.95427500	-0.55361500	18.14207900
C	7.59656600	6.27060000	20.04672800
H	8.36318700	6.95066400	20.38297900
N	11.28685800	4.43052000	18.90759000
C	14.60063500	7.18166700	16.59897300
N	12.40877400	3.73722500	18.57732800
C	13.22200500	7.42604000	16.63911400
H	12.70928600	8.36347600	16.52064700
N	11.08768100	3.91934800	15.64094300
C	11.00629300	4.11343600	20.17379000
H	10.13130300	4.52221000	20.65393400
N	12.25440800	3.33996200	16.03031900
C	14.75052200	5.82058400	16.80476700
H	15.63814900	5.21507400	16.84939100
C	11.94691800	3.21653700	20.68391300
H	11.98504500	2.78214700	21.66720900
N	15.64366700	8.13363200	16.38993300
N	8.19016200	9.16291500	16.68841900
C	12.81856200	3.00589300	19.63336700
H	13.69784500	2.38850300	19.56385700
N	7.81599200	7.86972600	16.90655100
C	10.66644700	3.23863400	14.57245800
H	9.73294100	3.49738500	14.09823000
C	11.55821600	2.21380000	14.25005100
H	11.48897400	1.50144600	13.44706100
N	10.43024400	9.20932200	17.84881800
N	10.26850400	8.81833700	15.30101900
C	6.49537500	7.86577300	16.98924900
H	5.93469700	6.96452100	17.15979400
C	12.55154400	2.31655100	15.20423000
H	13.44505500	1.73452400	15.35270500

N	10.47529600	7.97053300	18.40731000
N	10.27194400	7.46842200	15.13930700
C	6.01008500	9.16915400	16.82323800
N	4.64786200	9.59552100	16.84402500
C	7.12536200	9.96763300	16.63352100
H	7.20524300	11.02735800	16.46886300
C	11.16477900	8.09378400	19.54392700
H	11.36075800	7.22737800	20.15561200
C	11.56935600	9.41541300	19.74150800
H	12.13674900	9.82076800	20.56052000
C	11.08017700	10.08785000	18.63864900
H	11.14976400	11.12592700	18.36169800
C	10.81037400	7.23328100	13.94047500
H	10.94853200	6.22004200	13.59760400
C	11.15574500	8.42783400	13.30539700
H	11.60610500	8.55919000	12.33744000
C	10.79329600	9.40840000	14.20809400
H	10.87266100	10.48050400	14.14944700

Figure S26: B3LYP optimized ground state structure of and xyz coordinates for **Calc-1**. The global energy minimum for **Calc-1** was -2753.56 hartrees. No imaginary frequencies were generated using this model.

Table S1: TD-DFT B3LYP/def2-tzvp transitions for calculated excited states corresponding to UV-VIS and luminescence excitation bands.

Transition	Energy	Donor → Acceptor	Coefficient	Contribution	Oscillation
		187 → 206	0.22848	11%	
		188 → 206	-0.17307	7%	
		188 → 207	0.38406	32%	
		188 → 208	0.13366	4%	
$S_0 \rightarrow S_1$	314	189 → 207	-0.12677	4%	0.000
		189 → 208	-0.36474	29%	
		195 → 207	-0.12171	3%	
		196 → 206	-0.13392	4%	
		196 → 207	0.16549	6%	
		203 → 206	-0.17275	6%	
		203 → 207	0.21569	10%	
$S_0 \rightarrow S_7$	276 nm	204 → 206	0.21297	10%	0.0161
		205 → 207	0.40914	36%	
		205 → 208	0.42692	39%	
		179 → 206	0.43530	41%	
		179 → 208	0.22197	11%	
		180 → 206	-0.15601	5%	
$S_0 \rightarrow T_1$	404 nm	180 → 207	0.17855	7%	0.000
		181 → 206	0.21409	10%	
		181 → 207	0.11750	3%	
		181 → 208	0.30976	21%	
		185 → 206	-0.12354	3%	

Judd-Ofelt Analysis

Table 2: Judd-Ofelt parameters for **6a** and several Eu^{3+} complexes

Compound	Site Symmetry	Ω_2/ x10^{-20} cm^2	Ω_4/ x10^{-20} cm^2	Ω_6/ x10^{-20} cm^2
6a	D_{3h}	1.2	10.3	N/A
$[Eu_2(MELL)(H_2O)_6]^2$	D_{3h}	11.82	2.72	N/A
$[Eu(DPA)]^{3-,\,3}$	D_{3h}	10.5	5.31	8.32
$(BMIm)_2[Eu(Pic)_5]^4$	C_{4v}	15.1	13.9	N/A
$(BEIm)_2[Eu(Pic)_5]^4$	C_{4v}	12.0	10.3	N/A
$(BBIm)_2[Eu(Pic)_5]^4$	C_{4v}	9.6	9.2	N/A

a – Determined using JOES[5] with an assumed refractive index of 1.5.
MELL – mellitic acid, DPA – dipicolinic acid, pic – pircric acid, BMIM – 1-butyl,3-methylimidazolium, BEIM – 1-butyl,3-ethylimidazolium, BBIM – 1,3-dibutylimidazolium

The intensity of the hypersensitive $^5D_0 \rightarrow {}^7F_2$ transition can be used as a measure of the effect of the ligand field on Eu^{3+} and the JO parameter, Ω_2 is a numerical representation of said LF influence, aka covalency of Eu^{3+}—4-NO_2Tp^- bond. Ω_2 is associated with a dynamic coupling mechanism between the electric field of Ln^{3+} and the electric dipole of the ligand induced by the *f*-orbitals of Ln^{3+}. (see references 48 – 51 from the main text)

DC SQUID Data Fits and Parameters

Simulation of the temperature-dependent susceptibility data were accomplished using the PHI software.[6] The $|L, m_L, S, m_S>$ basis was used to describe the lanthanoid centers, and, given the local D_{3h} geometry of the coordination sphere, the crystal field was described by the Hamiltonian

$$\hat{H}_{CF} = B_2^0\theta_2\hat{O}_2^0 + B_4^0\theta_4\hat{O}_4^0 + B_6^0\theta_6\hat{O}_6^0 + B_6^6\theta_6\hat{O}_6^6$$

where B_k^q are the crystal field parameters (including orbital reduction parameters), θ_k are the operator equivalent factors and $\hat{O}_k^q$ the Stevens operator equivalents.[6-7]

For each complex, a full survey of the full B_k^q space between -5000 and +5000 cm^{-1} was conducted. The best fit between experimental data and simulation were scattered over the whole range for B_2^0 and B_4^0 but almost exclusively concentrated around 0 for B_0^6 and B_6^6. Therefore, in all further investigations, B_0^6 and B_6^6 were set to 0. The (B_2^0, B_4^0) space was surveyed in more detail, with the result represented Figure S27: Residual between experimental χmT data and simulation on a logarithmic scale for **4a.**Figure S27 - Figure *S29*.

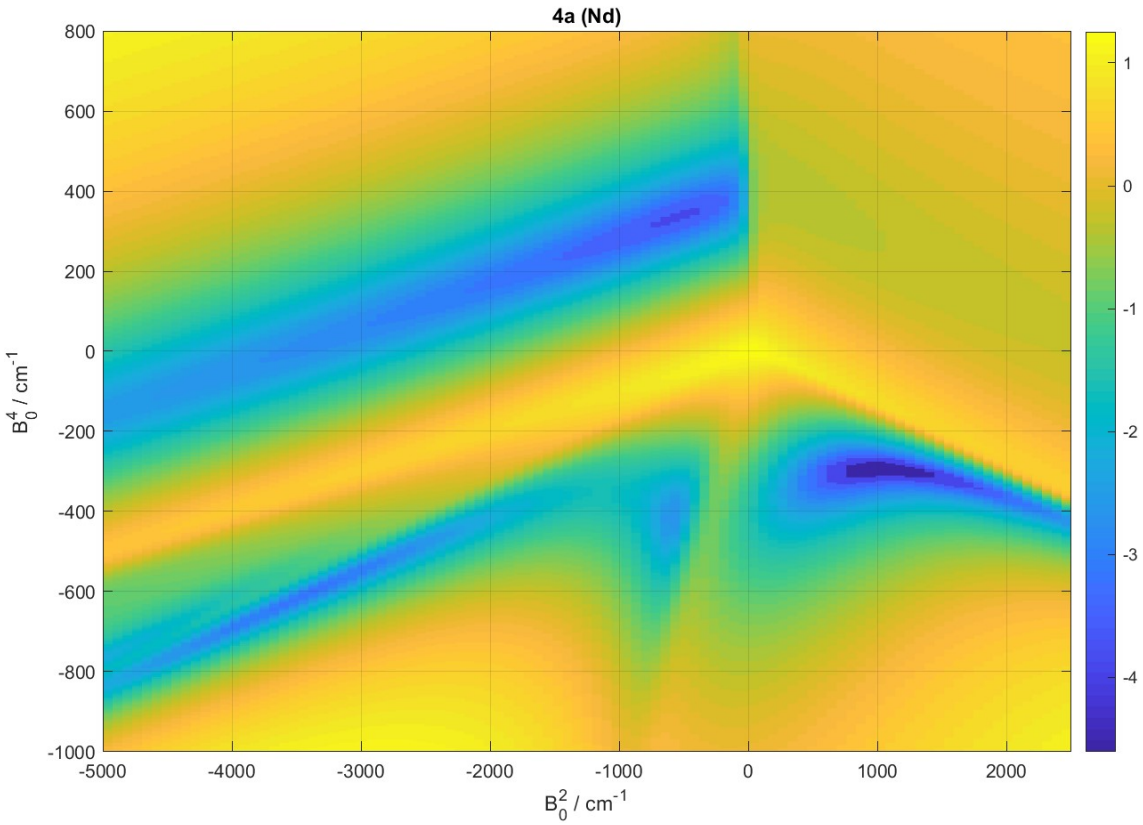

Figure S27: Residual between experimental $\chi_m T$ data and simulation on a logarithmic scale for **4a**.

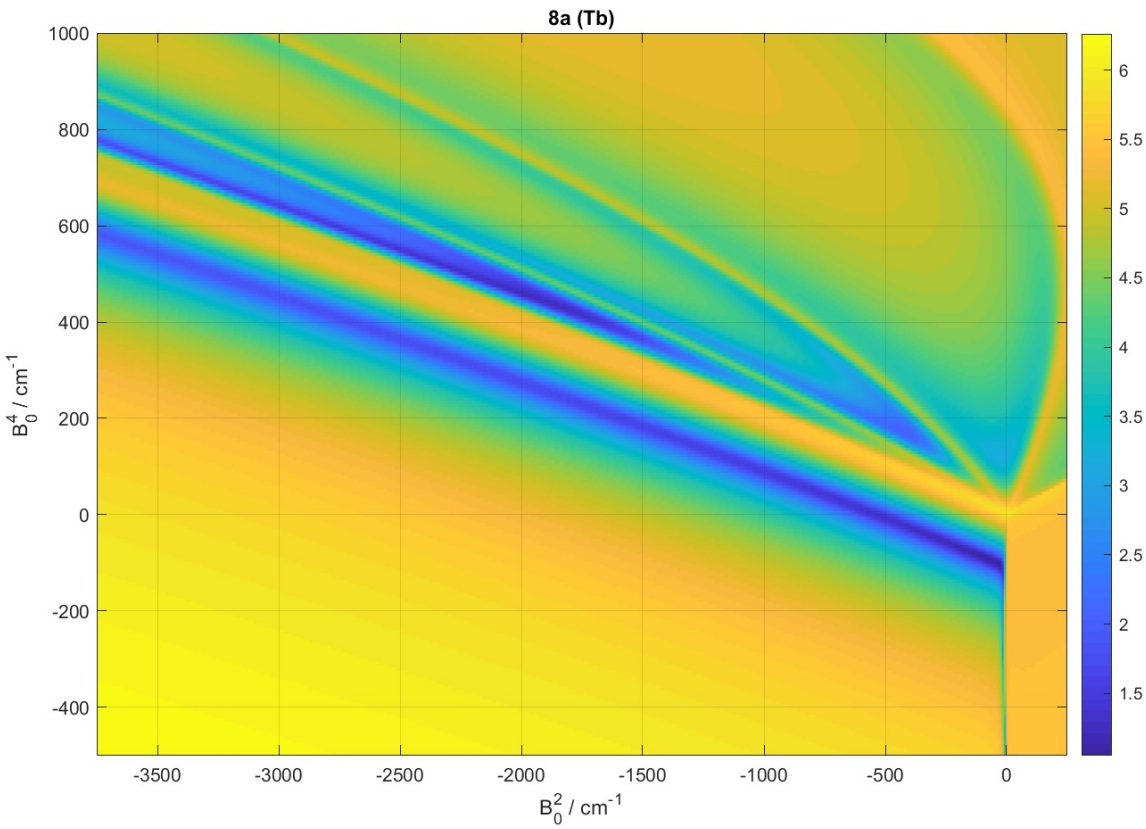

Figure S28: Residual between experimental $\chi_m T$ data and simulation on a logarithmic scale for **8a**.

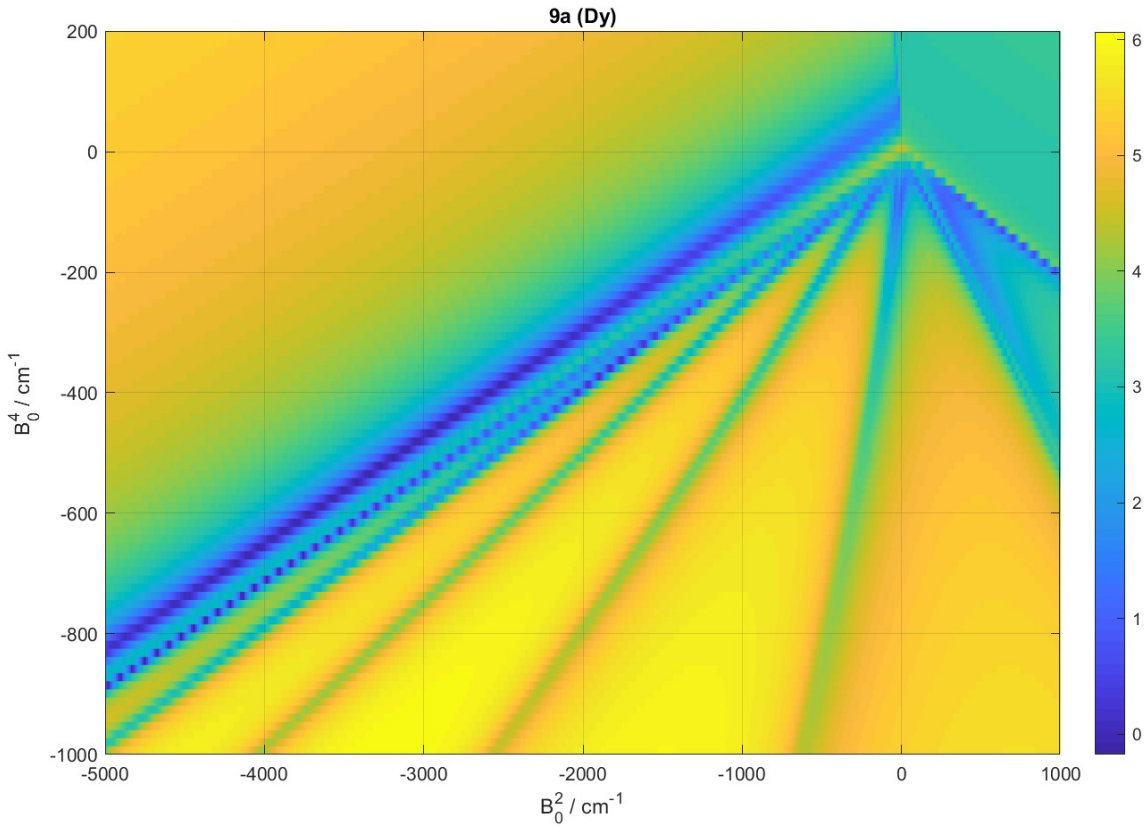

Figure S29: Residual between experimental $\chi_m T$ data and simulation on a logarithmic scale for **9a**.

Contours plots of all three surfaces were superimposed (), to allow the search of sets of crystal field parameters following a linear relationship with the number of 4f electrons in the complexes. Of the various combination of parameters investigated, only two gave satisfactory fits with the experimental data, and were manually optimized to give the two parameter sets (sets 1 and 2 on Figure S30 below) reported in the article.

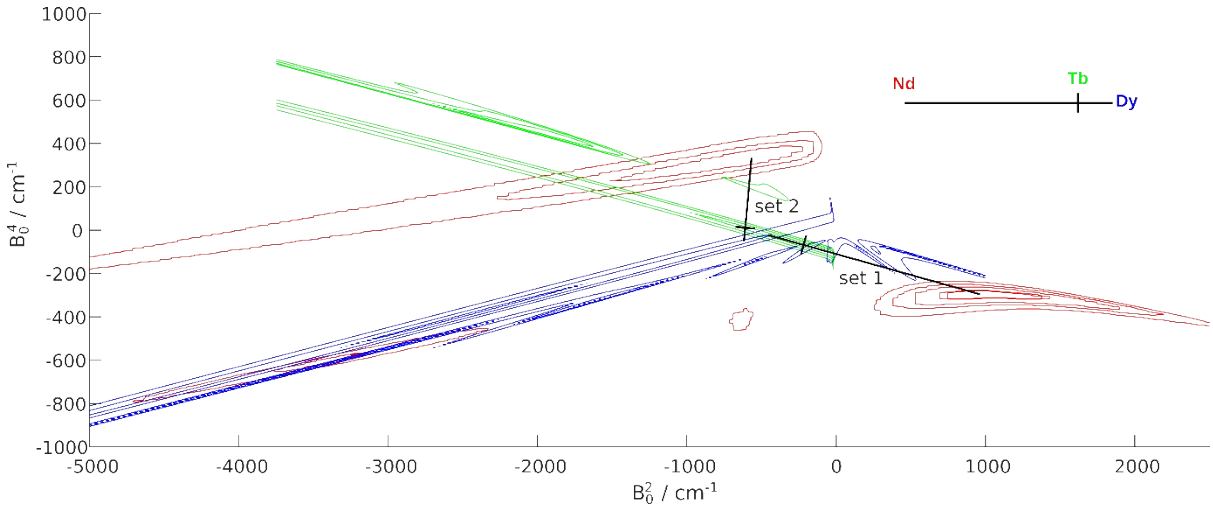

Figure S30: Contour plot corresponding to the surfaces represented in Figure S27 - Figure S29. The dagger marker is constrained at a 5:1 ratio to obtain a linear relationship between the crystal field parameters and the number of f electrons in the complex. The two best sets of parameters are marked on the figure.

AC SQUID Data Fits and Parameters

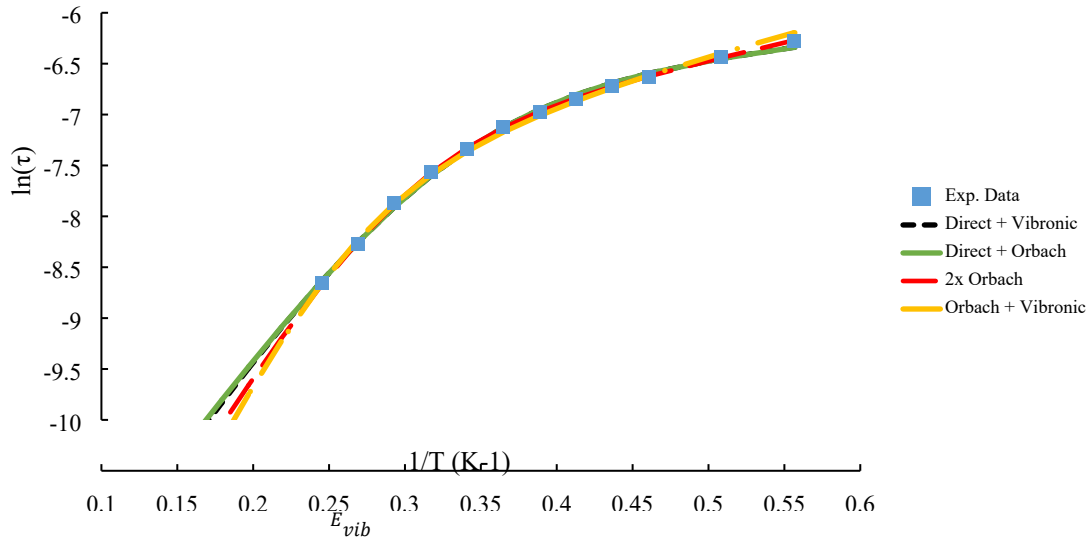

$$\tau^{-1} = AT + \tau_0^{-1} \frac{e^{\frac{E_{vib}}{k_B T}}}{\left(e^{\frac{E_{vib}}{k_B T}} - 1\right)^2} \qquad (1)$$

$$\tau^{-1} = AT + \tau_0^{-1} e^{-\frac{U_{eff}}{k_B T}} \qquad (2)$$

$$\tau^{-1} = \tau_0^{-1} e^{-\frac{U_{eff}}{k_B T}} + \tau_0^{'-1} e^{-\frac{U_{eff}^{'}}{k_B T}} \qquad (3)$$

$$\tau^{-1} = AT + \tau_0 e^{-\frac{U_{eff}}{k_B T}} + \tau_0^{'-1} \frac{e^{\frac{E_{vib}}{k_B T}}}{\left(e^{\frac{E_{vib}}{k_B T}} - 1\right)^2} \qquad (4)$$

Figure S31: Arrhenius plot of the magnetic relaxation time for **4a** with curves fits obtained using the equations, 1 – 4.

All of the above equations/models yield a satisfactory fit for the experimental data. Equation 1 was chosen to fit the data given the low value for U_{eff} ~ 14 cm^{-1} from all of the fits, is most likely a vibronic (two-phonons Raman relaxation) process and not a true Orbach barrier. Typical values for a real Orbach process would be >100 cm^{-1}.

References

1. Apostolidis, C.; Kovács, A.; Morgenstern, A. R., Jean; Walter, Olaf, Tris-{Hydridotris(1-pyrazolyl)borato}lanthanide Complexes: Synthesis, Spectroscopy, Crystal Structure and Bonding Properties. *Inorganics.* **2021,** *9* (6), 44. https://doi/10.3390/inorganics9060044.
2. Rodrigues, M. O.; Paz, F. A. A.; Freire, R. O.; de Sá, G. F.; Galembeck, A.; Montenegro, M. C. B. S. M.; Araújo, A. N.; Alves, S., Jr., Modeling, Structural, and Spectroscopic Studies of Lanthanide-Organic Frameworks. *J. Phys. Chem. B.* **2009,** *113* (36), 12181-12188. https://doi.org/10.1021/jp9022629.
3. Binnemans, K.; Van Herck, K.; Görller-Walrand, C., Influence of dipicolinate ligands on the spectroscopic properties of europium(III) in solution. *Chem. Phys. Lett.* **1997,** *266* (3), 297-302. https://doi.org/10.1016/S0009-2614(97)00012-2.
4. Borges, A. S.; Dutra, J. D. L.; Freire, R. O.; Moura, R. T., Jr.; Da Silva, J. G.; Malta, O. L.; Araujo, M. H.; Brito, H. F., Synthesis and Characterization of the Europium(III) Pentakis(picrate) Complexes with Imidazolium Countercations: Structural and Photoluminescence Study. *Inorg. Chem.* **2012,** *51* (23), 12867-12878. https://doi.org/10.1021/ic301776n.
5. Ćirić, A.; Stojadinović, S.; Sekulić, M.; Dramićanin, M. D., JOES: An application software for Judd-Ofelt analysis from Eu3+ emission spectra. *J. Lumin.* **2019,** *205*, 351-356. https://doi.org/10.1016/j.jlumin.2018.09.048.
6. Chilton, N. F.; Anderson, R. P.; Turner, L. D.; Soncini, A.; Murray, K. S., PHI: A powerful new program for the analysis of anisotropic monomeric and exchange-coupled polynuclear d- and f-block complexes. *J. Comp. Chem.* **2013,** *34* (13), 1164-1175. https://doi.org/10.1002/jcc.23234.
7. Bauer, E.; Rotter, M., MAGNETISM OF COMPLEX METALLIC ALLOYS: CRYSTALLINE ELECTRIC FIELD EFFECTS. In *Properties and Applications of Complex Intermetallics*, pp 183-248.